On-chip indistinguishable photons using III-V nanowire/SiN hybrid integration

Edith Yeung,[1,2] David B. Northeast,[1] Jeongwan Jin,[1] Patrick Laferrière,[1] Marek Korkusinski,[1,2] Philip J. Poole,[1]
Robin L. Williams,[1] and Dan Dalacu[1,2]
[1]*National Research Council Canada, Ottawa, Ontario, Canada K1A 0R6*
[2]*Department of Physics, University of Ottawa, Ottawa, Ontario, Canada K1N 6N5*

(Received 25 August 2023; accepted 1 November 2023; published 13 November 2023)

We demonstrate on-chip generation of indistinguishable photons based on a nanowire quantum dot. From a growth substrate containing arrays of positioned-controlled single-dot nanowires, we select a single nanowire which is placed on a SiN waveguide fabricated on a Si-based chip. Coupling of the quantum dot emission to the SiN waveguide is via the evanescent mode in the tapered nanowire. Postselected two-photon interference visibilities using continuous-wave excitation above band and into a p shell of the dot were 100% consistent with a single-photon source having negligible multiphoton emission probability. Visibilities over the entire photon wave packet, measured using pulsed excitation, were reduced by a factor of 5 when exciting quasiresonantly and by a factor of 10 for above-band excitation. The role of excitation timing jitter, spectral diffusion, and pure dephasing in limiting visibilities over the temporal extent of the photon is investigated using additional measurements of the coherence and linewidth of the emitted photons.

DOI: 10.1103/PhysRevB.108.195417

I. INTRODUCTION

High interference visibility between two single photons incident on separate input ports of a 50/50 beam splitter, i.e., the Hong-Ou-Mandel (HOM) effect [1], establishes the indistinguishable nature of the photons, an essential requirement in most photonic quantum technologies [2]. Epitaxial semiconductor quantum dots offer a solid-state solution for deterministically generating indistinguishable photons [3] with state-of-the-art sources demonstrating two-photon interference (TPI) visibilities in excess of 95% [4–6] for pulse separations of over 14 μs [7] in devices with efficiencies of up to 57% [8]. These sources were designed to emit out of plane, whereas a key advantage of solid-state emitters is the ability to integrate them with on-chip photonic circuitry [9]. An integrated platform, whereby multiple sources generate indistinguishable photons [10,11] propagating within on-chip photonic circuitry [12], is a long-term challenge addressing the scalability requirements of complex quantum processing schemes [2].

Two distinct technologies for generating on-chip indistinguishable photons using quantum dots are currently being pursued. In monolithic approaches [13], the quantum dot is embedded within photonic crystal waveguides [14,15] or suspended nanobeams [16] fabricated from the same III-V material system. Hybrid platforms [17], on the other hand, combine III-V-based quantum dot systems with Si-based integrated circuits in which the dot emission is coupled to waveguide structures using either direct butt-coupling [12] or evanescent fields [18]. Initial experiments [14–16,19] demonstrating the on-chip generation of indistinguishable photons using the above approaches relied on postselected TPI visibilities, where excitation was provided by a continuous-wave (cw) laser. More recently, nonpostselected measurements made using resonant pulsed excitation have shown TPI visibilities of $V > 90\%$ between sequentially emitted photons separated by a few nanoseconds [20–23] up to almost 800 ns [24].

In this work, we report on a deterministic hybrid technique for generating in-plane indistinguishable photons. We use position-controlled nanowire quantum dots [25] incorporated in photonic nanowire waveguides that are designed for efficient evanescent coupling to SiN waveguides [26]. The approach is similar to previous techniques employing evanescent coupling of III-V structures to underlying Si-based photonic structures [18,27,28], except here the adiabatic mode transfer is not realized through geometries defined by lithography, but rather by a taper introduced in the photonic nanowire during growth [29]. The hybrid construction relies on a pick and place technique, whereby individual nanowires are picked up from the III-V growth substrate and placed on a SiN waveguide fabricated on a Si wafer. The transfer is carried out in a scanning electron microscope (SEM) which provides a placement precision of a few nanometers, i.e., a positioning control sufficient to achieve optimal nanowire-waveguide coupling.

We obtain peak TPI visibilities of $V = 19.2\%$ over the temporal extent of the emitted photons when exciting nonresonantly. To gain insight into the the different mechanisms limiting the observation of high visibilities, we perform additional experiments sensitive to decoherence processes in two-level systems: first-order correlation, $g^{(1)}(\tau)$, and high-resolution spectroscopic measurements. These additional measurements point to fluctuations in the charge environment on timescales of <2 ns as the primary mechanism preventing the observation of high TPI visibilities, i.e., fluctuations expected when employing nonresonant excitation.

II. CHIP-INTEGRATED NANOWIRE SOURCE

The quantum dots used in this work are sections of InAsP incorporated within position-controlled InP nanowires

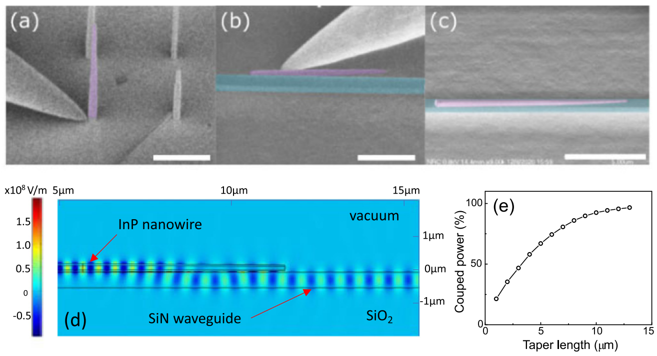

FIG. 1. Pick and place technique: (a) Nanowire (purple) picked up from growth substrate using a nanomanipulator probe. (b) Nanowire placed next to a SiN waveguide (blue). (c) Integrated InP nanowire-SiN ridge waveguide device. Scale bars are 5 μm. (d) Simulation of the electric field E_x of the fundamental waveguide mode propagating through a cross section of the hybrid device. (e) Calculated nanowire to waveguide mode coupling as a function of the nanowire taper length.

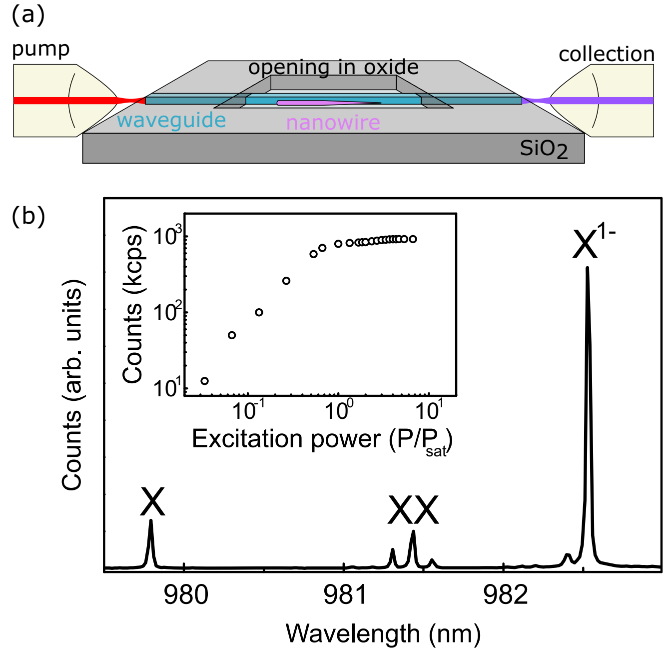

FIG. 2. (a) Schematic of the pump and collection scheme. (b) Photoluminescence spectrum from a hybrid integrated device. Inset: The detected count rates as a function of pump power using pulsed quasiresonant excitation at 80 MHz.

grown using gold-catalyzed vapor-liquid-solid epitaxy described in detail in Refs. [30–32]. The nanowires are clad with an InP shell to create a photonic nanowire with a base diameter of 250 nm that supports single-mode waveguiding of 1.3 eV photons. The photonic nanowire is tapered to a tip diameter of 100 nm over a ∼15 μm length [see Fig. 1(a)] to enable adiabatic mode transfer, discussed below. The low-loss photonic circuitry was fabricated in SiN grown by low-pressure chemical vapor deposition with measured propagation loss of ∼0.48 dB/cm at 965 nm. Waveguide dimensions were 400 nm wide and 485 nm thick with SiO_2 below and above, designed to support a single polarization mode at 1.3 eV. The SiN waveguides were terminated at etched facets of the Si chip where the width was tapered to 250 nm for efficient coupling to single-mode lensed fibers (SMLFs) with measured coupling losses of ∼2.15 dB/facet.

The nanowires were transferred to the Si chip prefabricated with the SiN photonic circuitry using an SEM-based nanomanipulator, as shown in Figs. 1(a)–1(c). A single nanowire is picked up from the growth substrate with a tungsten tip controlled by piezomotors and then moved to the Si chip mounted next to the growth substrate. The nanowire is then placed either on or beside a selected SiN waveguide which has been exposed by opening a 50×50 μm^2 window in the top oxide; see Fig. 2(a). As mentioned above, the nanowires are tapered to promote adiabatic mode transfer from the InP nanowire to the SiN waveguide. In Fig. 1(d), we show a simulation of the evanescent transfer of an appropriately polarized HE_{11} mode in the nanowire to the transverse magnetic mode in the SiN waveguide. From this, we calculate a transfer efficiency in excess of 90% for the nanowire geometry specified above; see Fig. 1(e).

The chip was cooled to 4 K in a fiber-coupled closed-cycle He cryostat equipped with *xyz* piezostages for fiber-waveguide alignment. The nanowires were optically excited through the waveguide via a SMLF. The emission was collected on the other end of the waveguide through another SMLF and directed to a fiber-coupled grating spectrometer equipped with a nitrogen-cooled charge-coupled device for spectrally resolved measurements or to superconducting nanowire single-photon detectors (SNSPDs, timing jitter 100 ps) via a fiber-coupled tunable filter (bandwidth = 0.1 nm) for measurements on single lines. An *s*-shell photoluminescence (PL) spectrum from the on-chip source is shown in Fig. 2(b) and displays the typical exciton complexes (X, XX, X^{1-}) observed from such nanowire quantum dots [33].

In this article, we focus on the X^{1-} emission. We first determine the efficiency of single-photon generation from the device. For pulsed above-band excitation at 80 MHz, we measure a maximum of 0.919 Mcps at the SNSPD at an excitation power $P = P_{\text{sat}}$ that saturates the transition; see inset in Fig. 2(b). Taking into account the optical throughput of the system (8.1%) and the detector efficiency (88.5%), both measured at 980 nm, we obtained a first-lens count rate of 12.9 Mcps, corresponding to source efficiency of $\eta_s \sim 16.1\%$. To estimate the dot to SiN waveguide coupling, we consider (i) a calculated dot-HE_{11} coupling of $\beta = 95\%$ [34], (ii) a 50% loss of photons for emission directed towards the base of the nanowire, (iii) a 50% loss due to the waveguide design which only supports one of the two polarization modes in the nanowire, and (iv) a 20% loss of photons emitted into phonon sidebands [34] which are filtered out. Taking into account these losses, we obtain an evanescent coupling efficiency of $\eta_c \sim 84.8\%$, slightly lower than both the calculations shown in Fig. 1(e) and our best measured results to date, $\eta_c \sim 93\%$ (see Ref. [35]). The lower-than-predicted values may be associated with emission into other charge complexes [25], e.g., the neutral complexes X and XX, evident in Fig. 2(b).

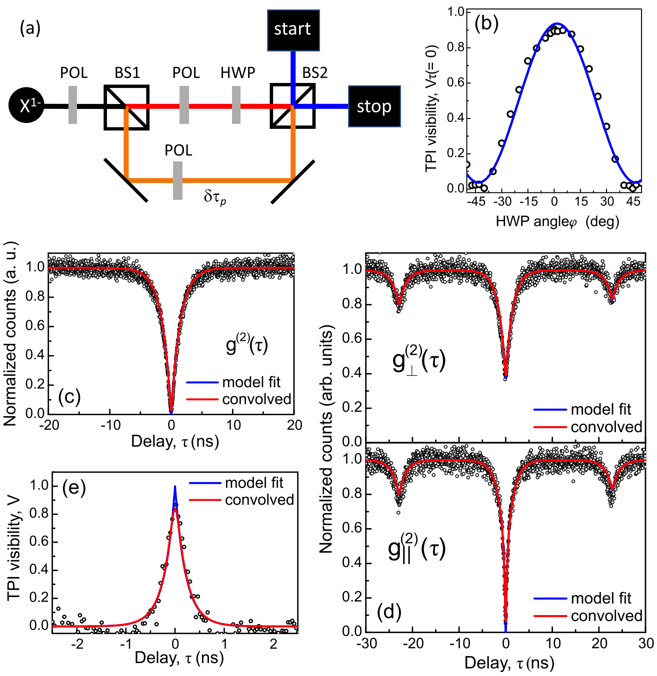

FIG. 3. (a) Schematic of Hong-Ou-Mandel (HOM) setup. (b) Raw TPI visibility at $\tau = 0$ ns as a function of HWP angle ϕ measured using above-band cw excitation at $P_{\rm sat}$ and a $\delta\tau_p = 1.84$ ns delay in one arm of the MZI. (c),(d) Correlation measurements performed with above-band cw excitation at $P_{\rm sat}/4$ and a $\delta\tau_p = 22.9$ ns delay. (e) Two-photon interference visibility calculated from (d). Black symbols: measured data. Blue curves: model fits described in the text. Red curves: after convolution with detector response.

III. TPI MEASUREMENTS: CW EXCITATION

In this section we describe the TPI measurements performed using cw excitation. This measurement provides information on the interference visibility between sequentially emitted photons where the experiment "selects" those photons that arrive at a beam splitter simultaneously. The extracted visibility is hence a visibility at a delay $\tau = 0$ and an ideal single-photon source, i.e., zero second-order correlations $g^{(2)}(\tau)$ at $\tau = 0$, should be 100%. Extracted values which are lower than this are due to the timing jitter in the detection system. We determine this zero-delay TPI visibility for different experimental conditions, including above-band and below-band excitation and as a function of the delay time between the two emitted photons.

To measure TPI visibilities, the polarization of the X^{1-} photons is first aligned to the slow axis of a polarization-maintaining (PM) fiber using a fiber paddle polarization controller and filtered using the tunable filter to isolate the X^{1-} line. The photons are then input to a PM fiber-based unbalanced Mach-Zehnder interferometer (MZI) equipped with two fiber-coupled free-space nonpolarizing beam splitters (BS1 and BS2), each with a 50:50 nominal splitting ratio; see Fig. 3(a). Two additional polarizers are placed on each arm of the MZI to ensure linear polarized photons incident on BS2. One arm of the MZI includes a half-wave plate (HWP) for controlling the relative polarizations, ϕ, of the photons incident on the input ports of BS2. The delay between the two arms of the interferometer, $\delta\tau_p$, is adjusted by adding additional fiber to one of the arms. Two SNSPD detectors at the output ports of BS2, labeled "start" and "stop," together with counting electronics are used to register coincidences.

We first verified the performance of the interferometer by measuring the dependence of the TPI visibility at $\tau = 0$ ns on ϕ, given by $V(0,\phi) = [g^{(2)}(0,\phi) - g^{(2)}(0,0^\circ)]/g^{(2)}(0,\phi)$. This is plotted in Fig. 3(b) (black symbols), measured using above-band cw excitation and a delay of $\delta\tau_p = 1.84$ ns. We observe an expected oscillatory behavior in the visibility, from $V \sim 0.9$ to $V \sim 0$, as ϕ is varied from 0° to $\pm 45^\circ$. The maximum observed visibility is limited by the detector response, discussed below.

To determine the TPI visibilities as a function of delay τ, coincidence spectra are measured for cross-linear ($\phi = 45^\circ$) and colinear ($\phi = 0^\circ$) polarized photons incident on BS2, $g_\perp^{(2)}(\tau)$ and $g_\parallel^{(2)}(\tau)$, respectively, and the visibilities are calculated from

$$V(\tau) = [g_\perp^{(2)}(\tau) - g_\parallel^{(2)}(\tau)]/g_\perp^{(2)}(\tau). \tag{1}$$

Typical spectra are shown in Fig. 3(d) (black symbols) for measurements made using above-band cw excitation at $P_{\rm sat}/4$ and a delay $\delta\tau_p = 22.9$ ns.

To model the coincidence spectra, we examine the four possible path combinations that two photons can take to traverse the MZI and simultaneously arrive at BS2 at $\tau = 0$. Consider first the two cases where the photons are incident on different input ports of BS2 (e.g., the photons travel in different arms of the MZI). If the pair is distinguishable (e.g., in the polarization degree of freedom by setting $\phi = 45^\circ$), each photon is equally likely to be reflected or transmitted, and of the four possible outcomes, only the two where the photons exit different ports will register coincidence counts at zero delay. This is the case in the upper panel of Fig. 3(d), which shows a $g_\perp^{(2)}(\tau = 0) \sim 0.5$ relative to the coincidence counts at long delays from uncorrelated photons. If the pair is indistinguishable, these two outcomes will destructively interfere (i.e., the incident pair coalesces, always exiting the same port) so that there are no possible outcomes that can register a coincidence at zero delay. This is the case in the lower panel of Fig. 3(d), which shows $g_\parallel^{(2)}(\tau = 0) \sim 0$. The other two cases, where the photons travel in the same arm of the MZI, will both have photons incident on the same port of BS2. Since the photons are generated by the same single-photon source, they cannot arrive simultaneously, and hence will not register zero-delay coincidences.

The absence of simultaneous photons incident on BS1 also eliminates one of the four possible outcomes that would lead to coincidences at $\tau = \pm\delta\tau_p$. This manifests as a reduction in $g^{(2)}(\tau)$ to $\sim$0.75 at $\tau = \pm\delta\tau_p$, which is seen in Fig. 3(d).

For 50:50 beam splitters, the behavior above can be modeled by

$$g_\perp^{(2)}(\tau) = \tfrac{1}{2} g^{(2)}(\tau) + \tfrac{1}{4}[g^{(2)}(\tau - \delta\tau_p) + g^{(2)}(\tau + \delta\tau_p)], \tag{2}$$

$$g_\parallel^{(2)}(\tau) = \frac{1}{2} g^{(2)}(\tau) + \frac{1}{4}[g^{(2)}(\tau - \delta\tau_p) + g^{(2)}(\tau + \delta\tau_p)] \times [1 - F e^{-2|\tau|/\tau_c'}], \tag{3}$$

which describe the cross-polarized, $g_{\perp}^{(2)}(\tau)$, and copolarized, $g_{\parallel}^{(2)}(\tau)$, coincidences, respectively, in terms of the second-order correlation function $g^{(2)}(\tau)$. The first (second) term in Eqs. (2) and (3) accounts for the cases where the photons are incident on the same (different) input port(s) of BS2, while F accounts for the spatial overlap of the photons on BS2 which is assumed to be 100% (i.e., $F = 1$). The timescale τ_c' represents, phenomenologically, the temporal extent over which photons incident on BS2 will coalesce, providing a measure of the probability of coalescence. The functional form with which it is incorporated in Eq. (3) will depend on the mechanism limiting coalescence, e.g., homogeneous versus inhomogeneous broadening. For simplicity, we use an exponential decay (i.e., the visibility is limited by pure dephasing [36]), though we do expect spectral diffusion to play a role due to the nonresonant excitation.

In this work, we use a modified model which explicitly includes the transmission (T_{BS1}, T_{BS2}) and reflection (R_{BS1}, R_{BS2}) coefficients of BS1 and BS2 [37],

$$\begin{aligned} g_{\perp}^{(2)}(\tau) =& 4\left(T_{\mathrm{BS1}}^2 + R_{\mathrm{BS1}}^2\right) R_{\mathrm{BS2}} T_{\mathrm{BS2}} g^{(2)}(\tau) \\ &+ 4 R_{\mathrm{BS1}} T_{\mathrm{BS1}} \left[T_{\mathrm{BS2}}^2 g^{(2)}(\tau - \delta\tau_p) \right. \\ &\left. + R_{\mathrm{BS2}}^2 g^{(2)}(\tau + \delta\tau_p)\right], \end{aligned} \tag{4}$$

$$\begin{aligned} g_{\parallel}^{(2)}(\tau) =& 4\left(T_{\mathrm{BS1}}^2 + R_{\mathrm{BS1}}^2\right) R_{\mathrm{BS2}} T_{\mathrm{BS2}} g^{(2)}(\tau) \\ &+ 4 R_{\mathrm{BS1}} T_{\mathrm{BS1}} \left[T_{\mathrm{BS2}}^2 g^{(2)}(\tau - \delta\tau_p) \right. \\ &\left. + R_{\mathrm{BS2}}^2 g^{(2)}(\tau + \delta\tau_p)\right] \times [1 - F e^{-2|\tau|/\tau_c'}]. \end{aligned} \tag{5}$$

The additional terms are required to account for deviations from a perfect, lossless system, i.e., deviations which result in coincidence dip depths that differ from the values described above. For example, if $T_{\mathrm{BS1}} \neq R_{\mathrm{BS1}}$, then the drop in coincidences at $\tau = \pm\delta\tau_p$ will be less than 25%, and, in the case of distinguishable photons, $g_{\perp}^{(2)}(\tau = 0) < 0.5$. For $T_{\mathrm{BS2}} \neq R_{\mathrm{BS2}}$, there will be an asymmetry in the depths of the $\tau = \pm\delta\tau_p$ side dips. Although there is little evidence of the latter in the measured spectra (i.e., $T_{\mathrm{BS2}} \sim R_{\mathrm{BS2}}$), we do observe values of $g_{\perp}^{(2)}(0) < 0.5$ which we associate not necessarily to an unbalanced BS1, but to a difference in the propagation losses between the two arms of the MZI (e.g., from inclusion of the components and accompanying mating sleeves) that result in different count rates incident on the two ports of BS2.

To reproduce the experimental $g_{\perp}^{(2)}(\tau)$ and $g_{\parallel}^{(2)}(\tau)$ using Eqs. (4) and (5), we first measure $g^{(2)}(\tau)$ by detecting coincidences at the two output ports of BS2. The $g^{(2)}(\tau)$ measured under the same operating conditions as the HOM experiment shown in Fig. 3(d) is shown in Fig. 3(c) (black symbols). The response is modeled using $g^{(2)}(\tau) = 1 - e^{-(1/T_1+R)|\tau|}$ (see the Supplemental Material [38]) where the radiative lifetime $T_1 = 1.75$ ns is independently measured and the excitation rate R is a fit parameter. The blue curve in the figure shows the model fit using $R = 0.1\ \mathrm{ns}^{-1}$.

This expression of $g^{(2)}(\tau)$ is incorporated in Eqs. (4) and (5), which are then applied to the measured correlations $g_{\perp}^{(2)}(\tau)$ and $g_{\parallel}^{(2)}(\tau)$, with τ_c' and the beam-splitter coefficients as fit parameters. The resulting fits are shown in Fig. 3(d) (blue curves) where, for this particular measurement (above-band cw excitation at $P_{\mathrm{sat}}/4$ and $\delta\tau_p = 22.9$ ns delay), we obtain a $T_{\mathrm{BS1}} : R_{\mathrm{BS1}}$ ratio of 0.25:0.75, a $T_{\mathrm{BS2}} : R_{\mathrm{BS2}}$ ratio of 0.48:0.52, and $\tau_c' = 0.55$ ns.

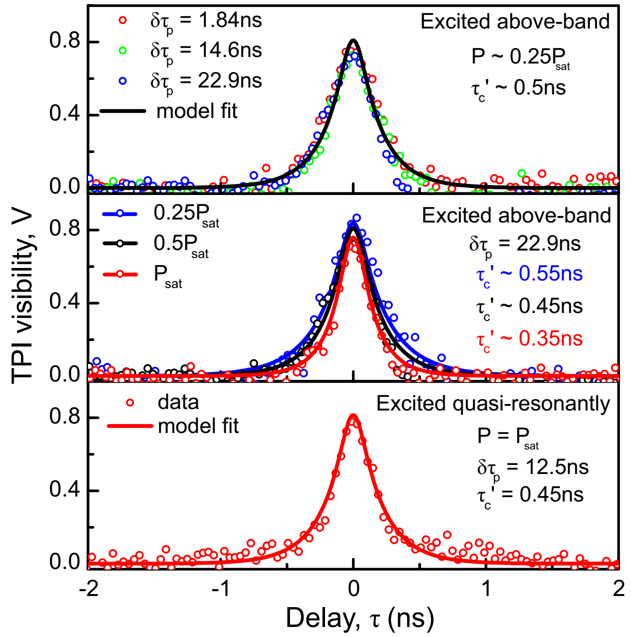

FIG. 4. TPI visibilities obtained under different operating conditions. Upper panel: visibilities using different delays $\delta\tau_{\mathrm{p}}$. Middle panel: visibilities as a function of excitation power. Lower panel: visibility under quasiresonant excitation into a p shell of the dot.

The visibility obtained from Eq. (1) using the model correlations is shown in Fig. 3(e) (blue curve) and, by definition, predicts a TPI visibility of $V(\tau = 0) = 1$. To match the experiment, we convolve the model correlations with a 100 ps Gaussian detector response function and obtain the red curves in Figs. 3(c)–3(e) which correctly predict the measured raw visibility of $V(\tau = 0) \sim 0.85$.

We have performed the above analysis on measurements taken under different operating conditions to extract τ_c' values. The results are summarized in Fig. 4. For measurements as a function of $\delta\tau_{\mathrm{p}}$ using above-band cw excitation at $P = 0.25P_{\mathrm{sat}}$ (upper panel), we obtained $\tau_c' \sim 0.5$ ns, independent of path delay for $\delta\tau_{\mathrm{p}} = 1.84$ to 22.9 ns. This suggests that the mechanisms limiting the τ_c' values occur on timescales faster than ∼2 ns. In contrast, from measurements as a function of excitation power (middle panel), we observed a significant increase in τ_c' from 0.35 to 0.55 ns for a fourfold reduction in power. We also observed a moderate increase in τ_c' when we excite quasiresonantly into a p shell of the dot. For measurements at $P = P_{\mathrm{sat}}$, $\tau_c' = 0.45$ ns for p-shell excitation (bottom panel) compared to $\tau_c' = 0.35$ ns for above-band excitation.

Although cw HOM measurements reveal the presence of decoherence mechanisms through the measurement of τ_c', the extraction of meaningful values requires simultaneous fitting of the three correlations $g^{(2)}(\tau)$, $g_{\perp}^{(2)}(\tau)$, and $g_{\parallel}^{(2)}(\tau)$ measured under the same operating conditions. Without the additional information provided by $g^{(2)}(\tau)$, erroneous values of τ_c' are possible due to the dependence of the antibunching dip in cw measurements on the excitation rate R; see, for example,

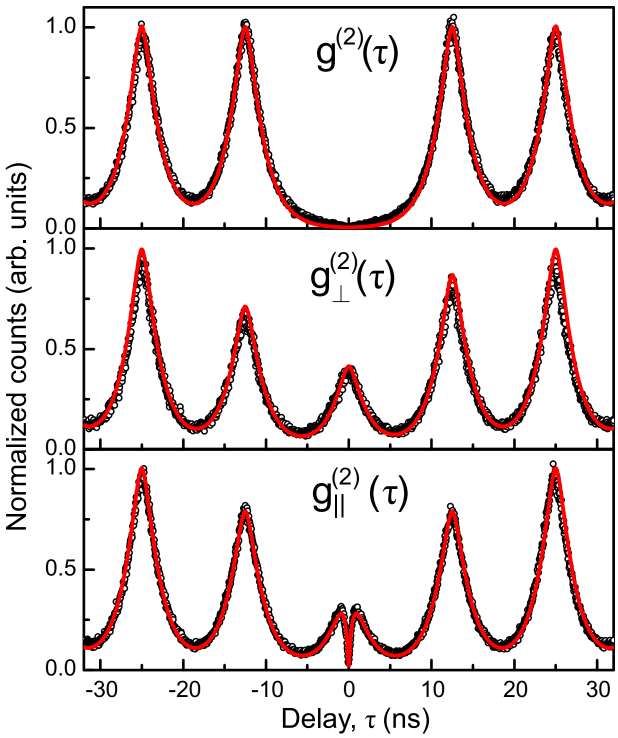

FIG. 5. Correlation measurements for quasiresonant pulsed excitation at $P_{\mathrm{sat}}/4$ (black symbols). Red curves are model fits described in the text.

Ref. [33] and the Supplemental Material [38], Fig. S1. Finally, we note that in all cases, $V(\tau = 0) = 1$ if account is taken of the detector response. This is expected in cw HOM measurements if $g^{(2)}(\tau = 0) = 0$, as is the case here, i.e., $V(\tau = 0)$ is only limited by the detector response [10,37,39].

IV. TPI MEASUREMENTS: PULSED EXCITATION

In this section, we repeat the above measurements but here we excited with a pulsed laser. Using pulsed excitation provides information on the TPI visibilities over the temporal extent of the emitted photons, e.g., nonpostselected. Unlike the cw measurements in the previous section, here we can quantify the probability of emitting identical photons. Excitation using a pulsed source will also be ultimately required for on-demand operation.

Using a tunable pulsed laser (pulse width ∼2 ps), we measure visibilities as in the previous section, for both above-band and quasiresonant excitation. We use a pulse repetition rate of 80 MHz, i.e., a pulse period of 12.5 ns, and a corresponding delay in one arm of the MZI of $\delta\tau_p = 12.5$ ns. The measured coincidences $g^{(2)}(\tau)$, $g_{\perp}^{(2)}(\tau)$, and $g_{\parallel}^{(2)}(\tau)$ (black symbols) for the case of quasiresonant excitation at $P_{\mathrm{sat}}/4$ are shown in Fig. 5.

Similar to the case of cw excitation for a nominal interferometer (50:50 beam splitters, 100% transmission), if two photons arriving simultaneously at BS2 are distinguishable, we expect a peak centered at zero delay having half the height of the peaks at $\pm 2T$ while the peaks at $\pm T$ should be reduced by 25%. For two perfectly indistinguishable photons arriving at BS2, the zero-delay peak should be absent. The measured $g_{\perp}^{(2)}(\tau)$ (middle panel in Fig. 5) qualitatively reproduces the behavior expected of impinging distinguishable photons on BS2. For the indistinguishable case, however, the zero-delay peak in the measured $g_{\parallel}^{(2)}(\tau)$ (bottom panel in Fig. 5) is still present, but with a dip that drops to zero coincidences at $\tau = 0$. This behavior is well documented [40–44] and is a consequence of processes that limit coalescence to timescales that are shorter than the temporal extent of the photons, e.g., (i) pure dephasing [45], (ii) spectral diffusion [46], and (iii) excitation timing jitter [47], and thus limit extracted τ_c' to values less than $2T_1$. We note that the last mechanism, i.e., timing jitter, is the primary distinction between the pulsed and cw measurements: it is absent in the latter where the experiment selects only the photons that arrive simultaneously at BS2.

As in the cw case, the curves in Fig. 5 are modeled using Eqs. (4) and (5), but with the latter modified to (see Supplemental Material [38])

$$\begin{aligned} g_{\parallel}^{(2)}(\tau) = {} & 4\left(T_{\mathrm{BS1}}^2 + R_{\mathrm{BS1}}^2\right) R_{\mathrm{BS2}} T_{\mathrm{BS2}} g^{(2)}(\tau) \\ & + 4 R_{\mathrm{BS1}} T_{\mathrm{BS1}} \big\{ \left[T_{\mathrm{BS2}}^2 g^{(2)}(\tau - \delta\tau_p) \right. \\ & \left. + R_{\mathrm{BS2}}^2 g^{(2)}(\tau + \delta\tau_p) \right] \\ & - \left[T_{\mathrm{BS2}}^2 g^{(2)}(-\delta\tau_p) + R_{\mathrm{BS2}}^2 g^{(2)}(+\delta\tau_p) \right] F e^{-2|\tau|/\tau_c'} \big\}, \end{aligned} \tag{6}$$

such that $g_{\parallel}^{(2)}(\tau)$ is simply given by $g_{\perp}^{(2)}(\tau)$ less the exponential term defining the timescale over which the photons coalesce. This is seen clearly for the case of nominal 50:50 beam splitters in which case Eq. (6) reduces to $g_{\perp}^{(2)}(\tau) - 0.5 F e^{-2|\tau|/\tau_c'}$ after setting $g^{(2)}(-\delta\tau_p) = g^{(2)}(+\delta\tau_p) = 1$.

The $g^{(2)}(\tau)$ that is incorporated in Eqs. (4) and (6) is constructed from peaks described by $e^{(-\tau/T_1)}[1 - e^{(-\tau/\tau_e)}] * e^{(\tau/T_1)}[1 - e^{(\tau/\tau_e)}]$, i.e., we self-convolve model fits to the measured time-resolved PL spectra; see the Supplemental Material [38], Fig. S2. This allows us to account for the dependence of the $g^{(2)}(\tau)$ peaks on operating conditions through τ_e, i.e., the timescale associated with preparation of the X^{1-} state. We neglect reexcitation which reduces the single-photon purity to ∼98% and assume a $g^{(2)}(\tau) = 0$ in the zero-delay peak. The resulting fits are shown in the figure (red curves) where, as for the cw measurements, we have fit the beam-splitter ratios and τ_c'. We note that for the pulsed measurements, we obtained slightly different beam-splitter ratios for cross- and colinear measurements, which is evident in the data from the pronounced asymmetry between the peaks at $\tau = \pm T$ in the $g_{\perp}^{(2)}(\tau)$ whereas these peaks are symmetric in the $g_{\parallel}^{(2)}(\tau)$ correlations. For the particular measurement shown in Fig. 5, i.e., quasiresonant excitation at $P_{\mathrm{sat}}/4$, we obtain a $T_{\mathrm{BS1}} : R_{\mathrm{BS1}}$ ratio of 0.27:0.73 (0.31:0.69) and $T_{\mathrm{BS2}} : R_{\mathrm{BS2}}$ ratio of 0.35:0.65 (0.5:0.5) for $g_{\perp}^{(2)}(\tau)$ [$g_{\parallel}^{(2)}(\tau)$] and $\tau_c' = 0.95$ ns.

In Fig. 6, we plot a zoom-in of the the zero-delay peaks for both cross- and colinear measurements, $g_{\perp}^{(2)}(\tau)$ and $g_{\parallel}^{(2)}(\tau)$, respectively, for quasiresonant (upper panel) and above-band (lower panel) excitation. The raw visibility over the temporal extent of the emitted photons is determined as in the previous section using Eq. (1), but here we use the integrated coincidence counts over $\tau \pm T/2$. Under quasiresonant

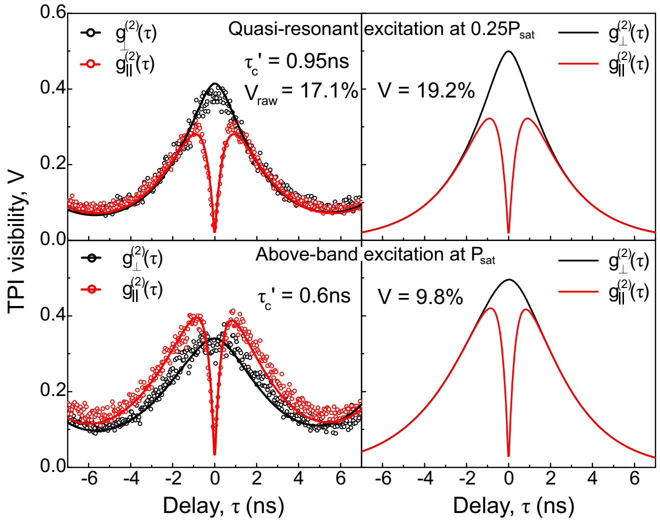

FIG. 6. Zero-delay correlation peaks under quasiresonant (upper panels) and above-band (lower panels) excitation. The left panels show the raw data (symbols) and model fits (curves). The right panels show the model calculations with BS1 and BS2 ratios set to 50:50 and contributions from side peaks removed.

excitation at $P = P_{\mathrm{sat}}/4$, we obtain a nonpostselected visibility of $V = 17.1\%$. If the contributions to the coincidence counts from the correlation side peaks are removed (see right panel of Fig. 6), we obtain a corrected visibility (e.g., the visibility that would result using a longer pulse period T) of $V = 19.2\%$. In this plot, we have also corrected for non-nominal values of the beam-splitter ratios for comparison with the above-band measurements, discussed below.

For above-band excitation (lower panel of Fig. 6), the zero-delay peak is significantly broader than that observed when exciting quasiresonantly [e.g., compare $g_\perp^{(2)}(\tau)$ (black curves)] and the dip at $\tau = 0$ is significantly narrower [compare $g_\parallel^{(2)}(\tau)$ (red curves)]. Both broadening of the peak and narrowing of the dip (quantified by the reduced $\tau_c' = 0.6$ ns) are a consequence of the more significant timing jitter [48] present in above-band excitation, i.e., longer timescale associated with the state preparation τ_e, since above-band excitation includes additional processes related to carrier thermalization and capture not present for quasiresonant excitation. We note that here we have used a higher excitation power than that used in the quasiresonant measurement and this will also contribute to a decrease in τ_c', as observed in the cw measurements.

We also observe that for the above-band measurements, the zero-delay peaks of cross- and colinear correlations do not overlap at τ values away from $\tau = 0$. This is a consequence of the more significant difference in the beam-splitter ratios between the respective measurements and strongly impacts the calculated visibility using the raw data. Instead, we calculate $g_\perp^{(2)}(\tau)$ and $g_\parallel^{(2)}(\tau)$ using the fit value of τ_c', but with 50:50 beam-splitter ratios as above. For the above-band nonpostselected visibility, we obtain $V = 9.2\%$, substantially lower compared to the quasiresonant case and consistent with the reduced τ' value.

Comparison with previously reported values is restricted due to the dependence of the measured visibilities on both excitation conditions [42,49] and the delay between interfered photons, $\delta\tau_p$ [50]. For above-band excitation, we refer to the reported values from our previous work [43] where visibilities of $V \sim 5\%$ were measured. There, a temporal delay of $\delta\tau_p = 50$ ns was used and the devices were grown at lower temperature where more severe linewidth broadening is expected; see Ref. [51]. In the case of p-shell excitation with $\delta\tau_p \sim 12.5$ ns, similar visibilities, in the range $V = 0.21$–0.59, have been previously reported [7,50,52], including from on-chip sources [20].

V. COHERENCE MEASUREMENTS

In this section, we determine the coherence properties of the two-level excitonic system. These measurements provide information on the factors (e.g., pure dephasing and charge noise) responsible for the low TPI visibilities observed in the previous section. We show results in the time domain where coherence times τ_c are extracted from single-photon interference visibilities, e.g., $g^{(1)}(\tau)$ measurements. We also compare with results in the frequency domain, where coherence times are extracted from linewidth measurements.

A. Interferometric measurements

For the time-domain measurements, the MZI was balanced (e.g., $\delta\tau_p = 0$) and a motorized fiber-based delay stage with a tuning range of 1.2 ns was added to one arm. The stage was scanned across its full range and, at selected delays $\delta\tau_p$, the fringe visibility was determined using a phase modulator in one arm of the MZI. The fringe visibility as a function of $\delta\tau_p$ extracted from above-band and quasiresonant measurements is plotted in Fig. 7.

For a homogeneously broadened transition, i.e., the spectral linewidth of the emitted photons corresponds to the natural linewidth, the line shape is Lorentzian and the visibility is expected to decay exponentially with a time constant T_2. In the presence of inhomogeneous broadening, the decay will have a Gaussian component [53], T_{G}, and is more appropriately described by a Voigt profile [43],

$$g^{(1)}(\delta\tau_p) \sim \exp\left[-\frac{\pi}{2}\left(\frac{\delta\tau_p}{T_{\mathrm{G}}}\right)^2 - \frac{|\delta\tau_p|}{T_2}\right]. \tag{7}$$

We model the above-band fringe visibility using Eq. (7) (curves in the upper panel of Fig. 7) to extract T_2 and T_{G}. To compare with the linewidth measurements below, we also calculated the full width at half maximum (FWHM) of the Voigt profile in the frequency domain given by

$$\delta\omega_{\mathrm{V}} = 0.535\delta\omega_{\mathrm{L}} + \sqrt{0.217\delta\omega_{\mathrm{L}}^2 + \delta\omega_{\mathrm{G}}^2}, \tag{8}$$

where $\delta\omega_{\mathrm{L}} = \frac{1}{\pi T_2}$ is the Lorentzian contribution to the linewidth and $\delta\omega_{\mathrm{G}} = \frac{\sqrt{2\ln 2}}{\sqrt{\pi}T_{\mathrm{G}}}$ is the Gaussian contribution. The extracted Voigt linewidths $\delta\omega_V$ using above-band excitation are plotted in Fig. 9 (filled symbols).

In the case of the quasiresonant measurements (lower panel of Fig. 7), instead of a simple decay in the visibility with

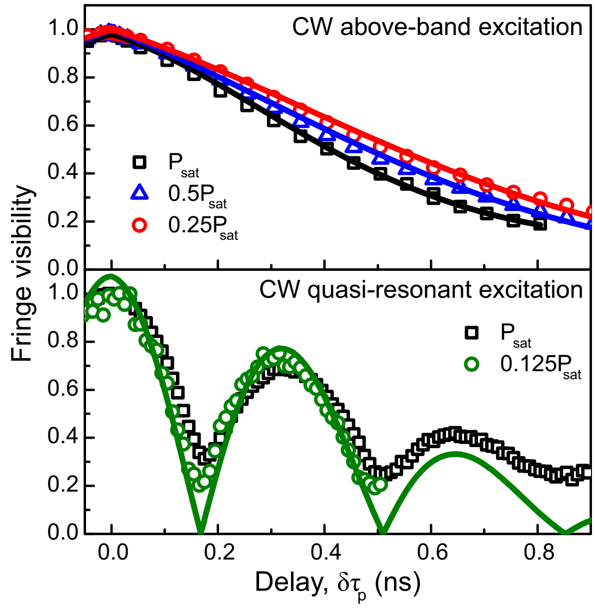

FIG. 7. Fringe visibility extracted from single-photon interference measurements using above-band (upper panel) and quasiresonant (lower panel) excitation. Curves are model fits described in the text.

$\delta\tau_p$, we observe oscillatory behavior indicative of a beating phenomenon. Why this arises is discussed below; here we simply assume the presence of two lines with frequency separation ω_s and identical coherence and model this behavior by multiplying Eq. (7) by the beating term $|\cos(\omega_s\delta\tau_p)|$. We only model the measurement at $P = 0.125P_{sat}$: at higher excitation powers (e.g., $P = P_{sat}$), the assumption of identical coherence properties likely does not apply, as suggested by the higher minima values in the visibility that are observed in the figure. The extracted $\delta\omega_V$ from Eq. (8) from the quasiresonant pump at $P = 0.125P_{sat}$ is plotted in Fig. 9 (open symbol).

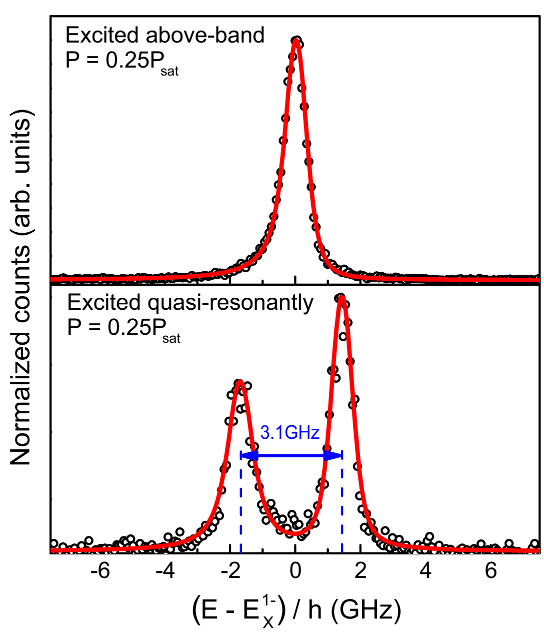

FIG. 8. High-resolution photoluminescence spectrum of the X^{1-} emission for cw above-band excitation (upper panel) and cw quasiresonant excitation (lower panel) at $P_{sat}/4$. Red curves are Voigt fits to the data.

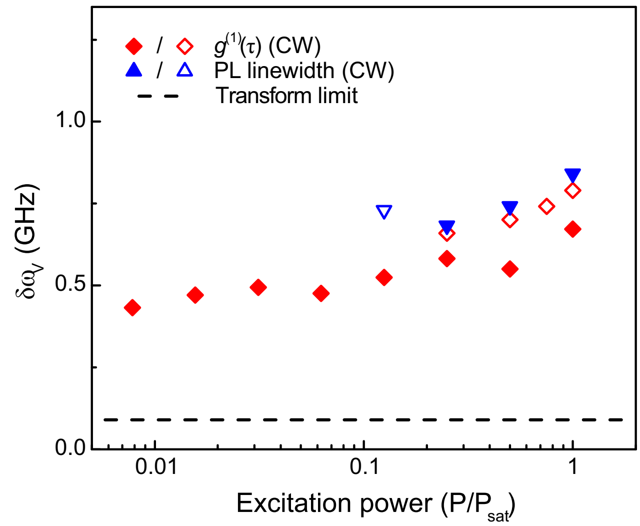

FIG. 9. Voigt linewidths extracted from $g^{(1)}(\tau)$ and high-resolution PL measurements as a function of excitation power. Filled (open) symbols correspond to above-band (quasiresonant) excitation. Dashed horizontal line indicates the transform-limited linewidth, $\delta\omega = 1/2\pi T_1$.

B. Linewidth measurements

In the frequency domain, we measure the linewidth of the emitted photons using a fiber-based, piezo-controlled Fabry-Perot etalon (bandwidth 250 MHz, free spectral range 40.75 GHz). High-resolution spectra obtained by scanning the etalon through the X^{1-} emission peak are shown in Fig. 8 for cw above-band (upper panel) and quasiresonant (lower panel) excitation at $P_{sat}/4$. For above-band excitation, we observe a single peak as expected from a singly charged complex, while for quasiresonant excitation, the same emission line is a doublet with a splitting of $\omega_s/\pi = 3.1$ GHz, consistent with the beating frequency observed in the coherence measurements. Given that $g^2(0) \sim 0$, the observation of two peaks suggests either two mutually exclusive excitonic complexes or the same excitonic complex with the electrostatic environment jumping between two possible states.

There are two possible reasons why the observation of either of the two complexes or the same complex in two environments would depend on the excitation energy. First, in quasiresonant excitation, fewer carriers are introduced into the system, resulting in a different Fermi level profile compared to above-band excitation. This may modify the relative intensities of different charge complexes in time-integrated PL spectra, which we have previously observed. Second, there may be a single, defect-related trap sufficiently close to the dot such that a Stark-mediated shift of the X^{-1} emission energy of $\omega_s \sim 3$ GHz will result, depending on the occupation of the trap. In this scenario, for above-band excitation, the trap occupation is constant on the timescale of the measurement ($\sim$100 ms), whereas for quasiresonant excitation, the occupation fluctuates on a much faster timescale such that both emission energies are observed in the time-integrated PL.

The magnitude of the observed splitting depends on the quasiresonant excitation power, decreasing by ~0.4 GHz as the power is increased from $0.25P_{\mathrm{sat}}$ to P_{sat}. Such an excitation power-dependent splitting is consistent with carrier screening of the Stark field, but difficult to explain in the case of two distinct complexes. We therefore attribute the two peaks observed when exciting quasiresonantly to the same excitonic complex X^{1-}.

High-resolution spectra were measured as a function of excitation power, deconvolved from the etalon response and fit using a Voigt line shape. We note that the line shapes obtained using above-band excitation present a slight asymmetry when excited at higher powers and these were fit with an asymmetric Voigt function. The origin of this asymmetry is unclear, but is typical of the nanowire quantum dot system [51]. The total linewidth $\delta\omega_V$ from the fits is plotted in Fig. 9 for both the above-band (filled) and quasiresonant (open) excitation. For clarity, only measurements of one of the two peaks observed with quasiresonant excitation are included (the power-dependent linewidths of the second peak are similar).

Comparison of the time- and frequency-domain measurements reveal similar linewidths which do not significantly depend on the excitation energy: above band (filled symbols) versus quasiresonant (open symbols). The absence of any narrowing when exciting below band is surprising: in fact, we observe a small increase in the measured linewidth for quasiresonant excitation. This suggests that the mechanisms responsible for the excess broadening are unrelated to the much higher density of excess carriers or phonons introduced with above-band excitation.

In all cases, we observe a decrease in excess broadening at lower excitation powers with a minimum extracted linewidth of 4X the transform limit (dashed line in Fig. 9). The reduction in linewidth with excitation power is expected from a reduction in both phonon-related pure dephasing and charge noise-related spectral diffusion. We do not attempt to quantify these two contributions in terms of the Lorentzian versus Gaussian contributions to the measured linewidth: although the total Voigt linewidth is considered accurate, the Lorentzian:Gaussian ratio likely has a large uncertainty.

VI. DISCUSSION

To compare the coherence measurements with the HOM results, we use T_2 and T_{G} extracted from the $g^{(1)}(\tau)$ and linewidth measurements to calculate a "coherence time" τ_c given by [46]

$$\tau_c = -\frac{T_{\mathrm{G}}^2}{\pi T_2} + \sqrt{\left(\frac{T_{\mathrm{G}}^2}{\pi T_2}\right)^2 + \frac{2T_{\mathrm{G}}^2}{\pi}}. \tag{9}$$

The calculated values of τ_c from the three experiments are summarized in Fig. 10. All measurements give τ_c values of 0.5 ± 0.1 ns at $P = P_{\mathrm{sat}}$, which increase as the excitation power is reduced, consistent with the linewidth measurements in Fig. 9, but still well below the transform limit of $2T_1$.

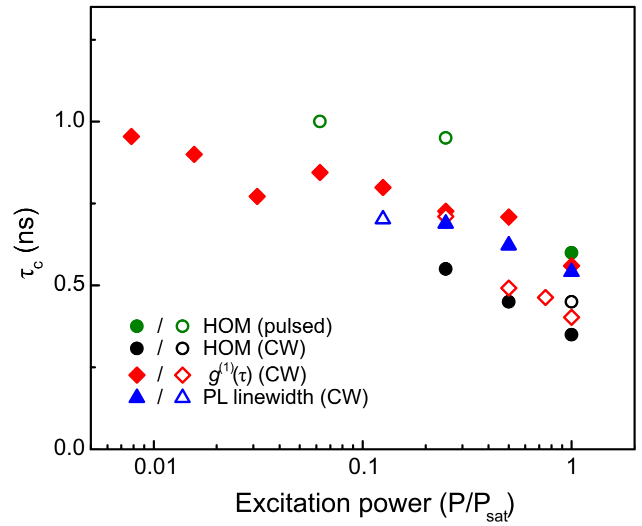

FIG. 10. Coherence times extracted from HOM, $g^{(1)}(\tau)$ and high-resolution PL measurements as a function of excitation power. Filled (open) symbols correspond to above-band (quasiresonant) excitation.

In the following, we consider the distinct nature of each experiment to extract information on the nature of the mechanisms responsible for $\tau_c < 2T_1$. We first consider the different timescales associated with each experiment. In the HOM measurement, different photons are interfered on a timescale of 2–23 ns, while in the coherence measurement, interference is between the same photon and the timescale is 1.2 ns, but each point in the fringe visibility trace is a statistical average over ~100 ms. In the linewidth measurements, on the other hand, there is no interference, only a measure of the spectral purity over timescales in the seconds. The consistency in the extracted coherence times irrespective of the experiment thus suggests that the mechanism(s) responsible for reducing values of τ_c below the transform limit of $2T_1$ occur on a timescale of <2 ns and there are no other mechanisms on longer timescales for at least seconds.

Next we note the absence of any significant improvement in τ_c when switching from above-band to quasiresonant excitation, which is in stark contrast to other studies [42]. This suggests that phonon dephasing is not the primary mechanism limiting the coherence times since the phonon occupation, by necessity, will be higher for above-band excitation [51], which leaves spectral diffusion as the likely source, meaning the charge environment is equally stable, regardless of excitation mode.

Finally, we note that all the measurements, with the exception of the pulsed HOM experiments, are independent of excitation jitter. And yet it is these measurements that produced the highest values of τ_c (compare, for example, pulsed versus cw HOM in Fig. 10). This suggests that either timing jitter is relatively unimportant or that pulsed excitation produces a more stable charge environment, thus compensating for any reduction in τ_c due to timing jitter.

VII. CONCLUSION

In summary, we have demonstrated the generation of indistinguishable photons on-chip based on the hybrid integration of position-controlled single quantum dot nanowires and silicon-based photonic integrated circuitry [26]. Nonpostselected measurements over the photon lifetime revealed coalescence of only a small fraction of the emitted photons, ∼20%. The TPI visibility was limited by the excess broadening that arises when exciting nonresonantly. Higher visibilities are anticipated with coherent excitation, as demonstrated in other quantum dot systems [4–6].

The described integration approach provides a route to developing a platform whereby multiple sources of indistinguishable photons can be selectively incorporated on-chip, a long-term goal of future quantum technologies. As a final note, in this work we investigated nanowire quantum dots emitting at $\lambda \sim 980$ nm. However, the InAs/InP material system is also the ideal choice for generating telecom wavelengths and we have recently demonstrated high-quality sources emitting in the O-band [54]. Using such emitters, the pick and place approach described here can be applied to the highly developed silicon-on-insulator integrated photonics platform.

The data that support the findings of this study are available from the corresponding author upon reasonable request.

ACKNOWLEDGMENTS

This work was supported by the Natural Sciences and Engineering Research Council of Canada through the Discovery Grant SNQLS, by the National Research Council of Canada through the Small Teams Ideation Program QPIC, and by the Canadian Space Agency through a collaborative project entitled “Field Deployable Single Photon Emitters for Quantum Secured Communications.” The authors would also like to thank Khaled Mnaymneh for assistance with the commercial foundry tape-out.

[1] C. K. Hong, Z. Y. Ou, and L. Mandel, Measurement of picosecond time intervals between two photons by interference, Phys. Rev. Lett. **59**, 2044 (1987).

[2] J. L. O’Brien, A. Furusawa, and J. Vučković, Photonic quantum technologies, Nat. Photon. **3**, 687 (2009).

[3] C. Santori, D. Fattal, J. Vučković, G. Solomon, and Y. Yamamoto, Indistinguishable photons from a single-photon device, Nature (London) **419**, 594 (2002).

[4] Y.-M. He, Y. He, Y.-J. Wei, D. Wu, M. Atatüre, C. Schneider, S. Höfling, M. Kamp, C.-Y. Lu, and J.-W. Pan, On-demand semiconductor single-photon source with near-unity indistinguishability, Nat. Nanotech. **8**, 213 (2013).

[5] X. Ding, Y. He, Z.-C. Duan, N. Gregersen, M.-C. Chen, S. Unsleber, S. Maier, C. Schneider, M. Kamp, S. Höfling, C.-Y. Lu, and J.-W. Pan, On-demand single photons with high extraction efficiency and near-unity indistinguishability from a resonantly driven quantum dot in a micropillar, Phys. Rev. Lett. **116**, 020401 (2016).

[6] N. Somaschi, V. Giesz, J.C. Loredo, M. P. Almeida, G. Hornecker, S.L. Portalupi, T. Grange, C. Antón, J. Demory, C. Gómez, I. Sagnes, N. D. Lanzillotti-Kimura, A. Lemaître, A. Auffèves, A. G. White, L. Lanco, and P. Senellart, Near-optimal single-photon sources in the solid state, Nat. Photon. **10**, 340 (2016).

[7] H. Wang, Z.-C. Duan, Y.-H. Li, Si Chen, J.-P. Li, Y.-M. He, M.-C. Chen, Y. He, X. Ding, C.-Z. Peng, C. Schneider, M. Kamp, S. Höfling, C.-Y. Lu, and J.-W. Pan, Near-transform-limited single photons from an efficient solid-state quantum emitter, Phys. Rev. Lett. **116**, 213601 (2016).

[8] N. Tomm, A. Javadi, N. O. Antoniadis, D. Najer, M. C. Löbl, Al. R. Korsch, R. Schott, S. R. Valentin, A. D. Wieck, A. Ludwig, and R. J. Warburton, A bright and fast source of coherent single photons, Nat. Nanotech. **16**, 399 (2021).

[9] S. Hepp, M. Jetter, S. L. Portalupi, and P. Michler, Semiconductor quantum dots for integrated quantum photonics, Adv. Quantum Technol. **2**, 1900020 (2019).

[10] R. B. Patel, A. J. Bennett, I. Farrer, C. A. Nicoll, D. A. Ritchie, and A. J. Shields, Two-photon interference of the emission from electrically tunable remote quantum dots, Nat. Photon. **4**, 632 (2010).

[11] J.-H. Kim, C. J. K. Richardson, R. P. Leavitt, and E. Waks, Two-photon interference from the far-field emission of chip-integrated cavity-coupled emitters, Nano Lett. **16**, 7061 (2016).

[12] D. J. P. Ellis, A. J. Bennett, C. Dangel, J. P. Lee, J. P. Griffiths, T. A. Mitchell, T.-K. Paraiso, P. Spencer, D. A. Ritchie, and A. J. Shields, Independent indistinguishable quantum light sources on a reconfigurable photonic integrated circuit, Appl. Phys. Lett. **112**, 211104 (2018).

[13] C. P. Dietrich, A. Fiore, M. G. Thompson, M. Kamp, and S. Höfling, Gaas integrated quantum photonics: Towards compact and multi-functional quantum photonic integrated circuits, Laser Photon. Rev. **10**, 870 (2016).

[14] S. Kalliakos, Y. Brody, A. Schwagmann, . J. Bennett, M. B. Ward, D. J. P. Ellis, J. Skiba-Szymanska, I. Farrer, J. P. Griffiths, G. A. C. Jones, D. A. Ritchie, and A. J. Shields, In-plane emission of indistinguishable photons generated by an integrated quantum emitter, Appl. Phys. Lett. **104**, 221109 (2014).

[15] S. Kalliakos, Y. Brody, A. J. Bennett, Da. J. P. Ellis, J. Skiba-Szymanska, I. Farrer, J. P. Griffiths, D. A. Ritchie, and A. J. Shields, Enhanced indistinguishability of in-plane single photons by resonance fluorescence on an integrated quantum dot, Appl. Phys. Lett. **109**, 151112 (2016).

[16] N. Prtljaga, C. Bentham, J. O’Hara, B. Royall, E. Clarke, L. R. Wilson, M. S. Skolnick, and A. M. Fox, On-chip interference of single photons from an embedded quantum dot and an external laser, Appl. Phys. Lett. **108**, 251101 (2016).

[17] A. W. Elshaari, W. Pernice, K. Srinivasan, O. Benson, and Val Zwiller, Hybrid integrated quantum photonic circuits, Nat. Photon. **14**, 285 (2020).

[18] P. Schnauber, J. Schall, S. Bounouar, T. Höhne, S.-I. Park, G.-H. Ryu, T. Heindel, S. Burger, J.-D. Song, S. Rodt, and S. Reitzenstein, Deterministic integration of quantum dots into on-chip multimode interference beam splitters using *in situ* electron beam lithography, Nano Lett. **18**, 2336 (2018).

[19] P. Schnauber, A. Singh, J. Schall, S.-I. Park, J.-D. Song, S. Rodt, K. Srinivasan, S. Reitzenstein, and M. Davanco,

Indistinguishable photons from deterministically integrated single quantum dots in heterogeneous GaAs/Si_3N_4 quantum photonic circuits, Nano Lett. **19**, 7164 (2019).

[20] G. Kiršanskė, H. Thyrrestrup, R. S. Daveau, C. L. Dreeßen, T. Pregnolato, L. Midolo, P. Tighineanu, A. Javadi, S. Stobbe, R. Schott, A. Ludwig, A. D. Wieck, S.-I. Park, J. D. Song, A. V. Kuhlmann, I. Söllner, M. C. Löbl, R. J. Warburton, and P. P. Lodahl, Indistinguishable and efficient single photons from a quantum dot in a planar nanobeam waveguide, Phys. Rev. B **96**, 165306 (2017).

[21] ÅĄ. Dusanowski, S.-H. Kwon, C. Schneider, and . Höfling, Near-unity indistinguishability single photon source for large-scale integrated quantum optics, Phys. Rev. Lett. **122**, 173602 (2019).

[22] R. Uppu, H. T. Eriksen, H. Thyrrestrup, A. D. Uğurlu, Y. Wang, S. Scholz, A. D. Wieck, A. Ludwig, M. C. Löbl, R. J. Warburton, P. Lodahl, and L. Midolo, On-chip deterministic operation of quantum dots in dual-mode waveguides for a plug-and-play single-photon source, Nat. Commun. **11**, 3782 (2020).

[23] ÅĄ. Dusanowski, D. Köck, E. Shin, S.-H. Kwon, C. Schneider, and S. Höfling, Purcell-enhanced and indistinguishable single-photon generation from quantum dots coupled to on-chip integrated ring resonators, Nano Lett. **20**, 6357 (2020).

[24] R. Uppu, F. T. Pedersen, . Wang, C. T. Olesen, C. Papon, X. Zhou, L. Midolo, S. Scholz, A. D. Wieck, A. Ludwig, and P. Lodahl, Scalable integrated single-photon source, Sci. Adv. **6**, eabc8268 (2020).

[25] P. Laferriére, E. Yeung, I. Miron, D. B. Northeast, S. Haffouz, J. Lapointe, M. Korkusinski, P. J. Poole, R. L. Williams, and D. Dalacu, Unity yield of deterministically positioned quantum dot single photon sources, Sci. Rep. **12**, 6376 (2022).

[26] K. Mnaymneh, D. Dalacu, J. McKee, J. Lapointe, S. Haffouz, J. F. Weber, D. B. Northeast, P. J. Poole, G. C. Aers, and R. L. Williams, On-chip integration of single photon sources via evanescent coupling of tapered nanowires to sin waveguide, Adv. Quantum Tech. **3**, 1900021 (2020).

[27] J.-H. Kim, S. Aghaeimeibodi, C. J. K. Richardson, R. P. Leavitt, D. Englund, and E. Waks, Hybrid integration of solid-state quantum emitters on a silicon photonic chip, Nano Lett. **17**, 7394 (2017).

[28] M. Davanco, J. Liu, L. Sapienza, C.-Z. Zhang, J. V. De Miranda Cardoso, V. Verma, R. Mirin, S. Nam, L. Liu, and K. Srinivasan, Heterogeneous integration for on-chip quantum photonic circuits with single quantum dot devices, Nat. Commun. **8**, 889 (2017).

[29] D. Dalacu, P. J. Poole, and R. L. Williams, Tailoring the geometry of bottom-up nanowires: Application to high efficiency single photon sources, Nanomater. **11**, 1201 (2021).

[30] D. Dalacu, A. Kam, D. G. Austing, X. Wu, J. Lapointe, G. C. Aers, and P. J. Poole, Selective-area vapour-liquid-solid growth of InP nanowires, Nanotechnol. **20**, 395602 (2009).

[31] D. Dalacu, K. Mnaymneh, X. Wu, J. Lapointe, G. C. Aers, P. J. Poole, and R. L. Williams, Selective-area vapor-liquid-sold growth of tunable InAsP quantum dots in nanowires, Appl. Phys. Lett. **98**, 251101 (2011).

[32] D. Dalacu, K. Mnaymneh, J. Lapointe, X. Wu, P. J. Poole, G. Bulgarini, V. Zwiller, and M. E. Reimer, Ultraclean emission from InAsP quantum dots in defect-free wurtzite InP nanowires, Nano Lett. **12**, 5919 (2012).

[33] P. Laferriére, E. Yeung, M. Korkusinski, P. J. Poole, R. L. Williams, D. Dalacu, J. Manalo, M. Cygorek, A. Altintas, and P. Hawrylak, Systematic study of the emission spectra of nanowire quantum dots, Appl. Phys. Lett. **118**, 161107 (2021).

[34] D. Dalacu, P. J. Poole, and R. L. Williams, Nanowire-based sources of nonclassical light, Nanotechnol. **30**, 232001 (2019).

[35] E. Yeung, Hybrid integration of quantum dot-nanowires with photonic integrated circuits, Master's thesis, University of Ottawa, 2021.

[36] J. Bylander, I. Robert-Philip, and I. Abram, Interference and correlation of two independent photons, Eur. Phys. J. D **22**, 295 (2003).

[37] R. B. Patel, A. J. Bennett, K. Cooper, P. Atkinson, C. A. Nicoll, D. A. Ritchie, and A. J. Shields, Postselective two-photon interference from a continuous nonclassical stream of photons emitted by a quantum dot, Phys. Rev. Lett. **100**, 207405 (2008).

[38] See Supplemental Material at http://link.aps.org/supplemental/10.1103/PhysRevB.108.195417 for additional measurements.

[39] S. Ates, S. M. Ulrich, S. Reitzenstein, A. Löffler, A. Forchel, and P. Michler, Post-selected indistinguishable photons from the resonance fluorescence of a single quantum dot in a microcavity, Phys. Rev. Lett. **103**, 167402 (2009).

[40] E. B. Flagg, A. Muller, S. V. Polyakov, A. Ling, A. Migdall, and G. S. Solomon, Interference of single photons from two separate semiconductor quantum dots, Phys. Rev. Lett. **104**, 137401 (2010).

[41] P. Gold, A. Thoma, S. Maier, S. Reitzenstein, C. Schneider, S. Höfling, and M. Kamp, Two-photon interference from remote quantum dots with inhomogeneously broadened linewidths, Phys. Rev. B **89**, 035313 (2014).

[42] T. Huber, A. Predojević, D. Föger, G. Solomon, and G. Weihs, Optimal excitation conditions for indistinguishable photons from quantum dots, New J. Phys. **17**, 123025 (2015).

[43] M. E. Reimer, G. Bulgarini, A. Fognini, R. W. Heeres, B. J. Witek, M. A. M. Versteegh, A. Rubino, T. Braun, M. Kamp, S. Höfling, D. Dalacu, J. Lapointe, P. J. Poole, and V. Zwiller, Overcoming power broadening of the quantum dot emission in a pure wurtzite nanowire, Phys. Rev. B **93**, 195316 (2016).

[44] J. H. Weber, J. Kettler, H. Vural, M. Müller, J. Maisch, M. Jetter, S. L. Portalupi, and P. Michler, Overcoming correlation fluctuations in two-photon interference experiments with differently bright and independently blinking remote quantum emitters, Phys. Rev. B **97**, 195414 (2018).

[45] T. Legero, T. Wilk, A. Kuhn, and G. Rempe, Time-resolved two-photon quantum interference, Appl. Phys. B **77**, 797 (2003).

[46] B. Kambs and C. Becher, Limitations on the indistinguishability of photons from remote solid state sources, New J. Phys. **20**, 115003 (2018).

[47] A. Kiraz, M. Atatüre, and A. Imamoglu, Quantum-dot single-photon sources: Prospects for applications in linear optics quantum-information processing, Phys. Rev. A **69**, 032305 (2004).

[48] T. Legero, T. Wilk, A. Kuhn, and G. Rempe, Characterization of single photons using two-photon interference, Adv. At. Mol. Opt. Phys. **53**, 253 (2006).

[49] M. Reindl, J. H. Weber, D. Huber, C. Schimpf, S. F. C. da Silva, S. L. Portalupi, R. Trotta, P. Michler, and A. Rastelli, Highly indistinguishable single photons from incoherently excited quantum dots, Phys. Rev. B **100**, 155420 (2019).

[50] A. Thoma, P. Schnauber, M. Gschrey, M. Seifried, J. Wolters, J.-H. Schulze, A. Strittmatter, S. Rodt, A. Carmele, A. Knorr, T. Heindel, and S. Reitzenstein, Exploring dephasing of a solid-state quantum emitter via time- and temperature-dependent Hong-Ou-Mandel experiments, Phys. Rev. Lett. **116**, 033601 (2016).

[51] P. Laferrière, A. Yin, E. Yeung, L. Kusmic, M. Korkusinski, P. Rasekh, D. B. Northeast, S. Haffouz, J. Lapointe, P. J. Poole, R. L. Williams, and D. Dalacu, Approaching transform-limited photons from nanowire quantum dots excited above-band, Phys. Rev. B **107**, 155422 (2023).

[52] M. Gschrey, A. Thoma, P. Schnauber, M. Seifried, R. Schmidt, B. Wohlfeil, L. Krüger, J.-H. Schulze, T. Heindel, S. Burger, F. Schmidt, A. Strittmatter, S. Rodt, and S. Reitzenstein, Highly indistinguishable photons from deterministic quantum-dot microlenses utilizing three dimensional in situ electron-beam lithography, Nat. Commun. **6**, 7662 (2015).

[53] A. Berthelot, I. Favero, G. Cassabois, C. Voisin, C. Delalande, Ph. Roussignol, R. Ferreira, and J. M. Gérard, Unconventional motional narrowing in the optical spectrum of a semiconductor quantum dot, Nat. Phys. **2**, 759 (2006).

[54] P. Laferrière, S. Haffouz, D. B. Northeast, P. J. Poole, and R. L. W. D. Dalacu, Position-controlled telecom single photon emitters operating at elevated temperatures, Nano Lett. **23**, 962 (2023).